


 Cite this: *Nanoscale*, 2025, **17**, 7164

## Quantitative comparison of local field enhancement from tip-apex and plasmonic nanofocusing excitation *via* plasmon-assisted field emission resonances†

 Chenfang Lin,<sup>id</sup>\*<sup>a</sup> Jie Li,<sup>a</sup> Guoao Li,<sup>a</sup> Wenjie Luo,<sup>a</sup> Shuyi Liu,<sup>b</sup> Adnan Hammud,<sup>c</sup> Yang Xia,<sup>a</sup> Anlian Pan,<sup>id</sup><sup>a,d</sup> Martin Wolf,<sup>id</sup><sup>e</sup> Melanie Müller<sup>id</sup><sup>e</sup> and Takashi Kumagai<sup>id</sup>\*<sup>f,g</sup>

Plasmonic nanofocusing *via* off-site excitation offers a promising approach to minimize background light scattering and enhance excitation efficiency in tip-enhanced optical spectroscopy. However, a comprehensive understanding of its effectiveness compared to direct tip-apex excitation remains limited. Here we introduce plasmon-assisted field emission resonances as a practicable approach for quantitative evaluation of the local field enhancement in a scanning-tunneling-microscope junction *via* off-site excitation compared to direct tip-apex excitation. By using single-groove pyramidal tips suitable for multi-wavelength excitations, we find that the near-field intensity is approximately 3.8 and 1.7 times higher for off-site excitation than for direct apex excitation at excitation wavelengths of 780 nm and 633 nm, respectively. These results are further supported by numerical electromagnetic field simulations. Our findings demonstrate the effective implementation of plasmonic nanofocusing in low-temperature scanning tunneling microscopy, paving the way for more precise and background-free tip-enhanced optical spectroscopy at the atomic scale.

 Received 15th October 2024,  
 Accepted 16th February 2025

DOI: 10.1039/d4nr04262j

[rsc.li/nanoscale](https://rsc.li/nanoscale)

### 1. Introduction

Integrating optical excitation and photon detection into cryogenic ultrahigh-vacuum (UHV) scanning tunneling microscopes (STM) has enabled tip-enhanced optical spectroscopy with exceptional sensitivity and spatial resolution, providing unprecedented opportunities to study light-matter interactions and

material properties at the nanoscale and beyond.<sup>1–4</sup> Recent advances include Raman and photoluminescence mapping with sub-molecular resolution,<sup>2–4</sup> imaging of photocurrent distributions through molecular orbitals,<sup>5</sup> control of single-molecule reactions,<sup>6,7</sup> and the investigation of nanoscale heating.<sup>8,9</sup> A significant advancement has been the stable formation of atomic-scale protrusions at the tip apex, creating “picocavities”<sup>10,11</sup> within the STM junction under cryogenic UHV conditions,<sup>4</sup> which play crucial roles in achieving atomic-scale sensitivity and resolution.<sup>12</sup> While the picocavities enable atomic-scale localization of optical fields, the near-field enhancement and spectral distribution are also influenced by the nano- to mesoscale structure of the tip shaft and apex<sup>4,11,13,14</sup> and the excitation schemes.<sup>15,16</sup> In addition to improving control over the atomistic tip structure, optimization of the excitation efficiency of localized surface plasmons (LSPs) in the STM junction and its accurate characterization is highly desired to further advance optical spectroscopy at atomic scales.

An advanced approach for optimizing and controlling the generation of near fields in tip-enhanced optical spectroscopy is an off-site generation of LSPs *via* excitation of propagating surface plasmon polaritons (SPPs) and their adiabatic compression along the tapered tip shaft, followed by nanofocusing into the tip apex (Fig. 1a).<sup>15,17–20</sup> Broadband SPP excitation and

<sup>a</sup>Key Laboratory for Micro-Nano Physics and Technology of Hunan Province, State Key Laboratory of Chemo/Biosensing and Chemometrics, Hunan Institute of Optoelectronic Integration, College of Materials Science and Engineering, Hunan University, 410082 Changsha, China. E-mail: [lincf@hnu.edu.cn](mailto:lincf@hnu.edu.cn)

<sup>b</sup>Wuhan National Laboratory for Optoelectronics, Huazhong University of Science and Technology, Wuhan, 430074 China

<sup>c</sup>Department of Inorganic Chemistry, Fritz Haber Institute of the Max Planck Society, Faradayweg 4-6, 14195 Berlin, Germany

<sup>d</sup>School of Physics and Electronics, Hunan Normal University, 410081 Changsha, China

<sup>e</sup>Department of Physical Chemistry, Fritz Haber Institute of the Max Planck Society, Faradayweg 4-6, 14195 Berlin, Germany

<sup>f</sup>Institute for Molecular Science, 38 NishigoNaka, Myodaiji, Okazaki 444-8585, Japan. E-mail: [kuma@ims.ac.jp](mailto:kuma@ims.ac.jp)

<sup>g</sup>The Graduate University for Advanced Studies, SOKENDAI, Hayama, Kanagawa 240-0193, Japan

†Electronic supplementary information (ESI) available. See DOI: <https://doi.org/10.1039/d4nr04262j>

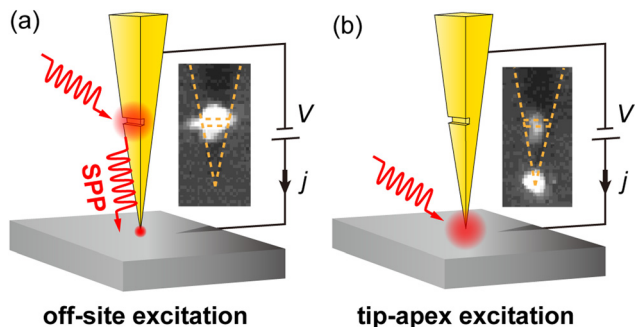


Fig. 1 Schematic off-site (a) and tip-apex (b) excitation. Inset: optical image of light scattering under groove and apex illumination.

nanofocusing have been demonstrated using single grooves,<sup>21</sup> grating couplers,<sup>19,22</sup> or thin films<sup>23</sup> fabricated into/onto the SPM tip shaft, increasing the local field enhancement and far-field to near-field conversion efficiency compared to direct tip-apex illumination.<sup>18,24,25</sup> Furthermore, SPP nanofocusing allows elimination of the unwanted far-field background scattering signals in tip-enhanced optical spectroscopy,<sup>16,26,27</sup> and has been employed for nonlinear nano-spectroscopic imaging.<sup>28–31</sup>

While off-site excitation schemes employing SPP nanofocusing have been extensively explored in tip-enhanced optical spectroscopy based on atomic force microscopy under ambient conditions,<sup>16,20,21,23,31–36</sup> their application in low-temperature STM for atomic-scale optical spectroscopy has only recently been initiated,<sup>37</sup> and remains underdeveloped. While far-field background is not very critical in tip-enhanced Raman spectroscopy of submonolayer molecules<sup>38</sup> or 2D materials<sup>39,40</sup> on Au or Ag substrates, background scattering becomes a significant problem when conducting tip-enhanced photoluminescence spectroscopy of 2D materials<sup>41</sup> and atomic-scale optical spectroscopy on the surface of bulk solids.<sup>42</sup> In the latter case, the implementation of off-site excitation scheme in STM-based atomic-scale optical spectroscopy may be preferable. The off-site excitation scheme may also be advantageous to enhance sensitivity in elastic near-field scattering, which can suffer from

interference with the background from far-field.<sup>42</sup> In addition, efficient off-site excitation of the LSP in STM could be advantageous for ultrafast STM to reduce background photoemission currents and to enable the local optical excitation of the sample without large-scale sample illumination.

To evaluate SPP nanofocusing in low-temperature STM, an *in situ* evaluation method to quantitatively compare the field enhancement generated by off-site *versus* tip-apex excitation of LSPs within the STM junction is needed. Two experimental approaches are available for this purpose: (1) detection of elastically or inelastically scattered light; (2) measuring photo-induced tunneling currents. Inelastic light scattering, such as tip-enhanced Raman spectroscopy, is often employed to evaluate the near-field intensity within STM junctions.<sup>16,43</sup> In addition, photoemission current excited by femtosecond laser from free-standing nanotips<sup>44,45</sup> or STM tips<sup>37,46</sup> allows evaluation of the near-field intensity achieved by SPP nanofocusing.

Here, we introduce an additional approach for evaluating the field enhancement in plasmonic STM junctions using plasmon-assisted field emission resonances (FERs).<sup>47</sup> This method offers a practical and reliable approach for *in situ* characterization of the near-field intensity during STM operation. Specifically, we demonstrate that it allows quantifying the relative field enhancement of direct tip-apex illumination *versus* off-site excitation of the LSP inside an Au-tip – Ag(111)-substrate junction. The intensity of the plasmon-assisted FERs, which are probed by highly localized tunneling current,<sup>47</sup> serve as a sensitive probe for the near-field intensity inside the STM junction. Compared to photoemission currents,<sup>37,44–46</sup> plasmon-assisted FERs are generated by one-photon absorption, *i.e.*, a linear process, making it more accessible within the intensity range available in tip-enhanced Raman and photoluminescence spectroscopy.<sup>48</sup> In contrast to previous studies which employed a grating coupler for off-site excitation and comparison of the resulting field enhancement with direct apex illumination,<sup>16,44</sup> our work uses a single-groove coupler. This is a simplified version of a grating for sufficiently small laser spot sizes comparable to the groove size and has been employed to generate white “nanolight”.<sup>21</sup> However, a direct comparison of the near-field enhancement achieved by a single-groove coupler with that of direct tip-apex illumination has not been carefully investigated.



Chenfang Lin

Chenfang Lin obtained his Ph.D. from Peking University, China, in 2015. He then became a postdoctoral researcher at the University of Liverpool, and later at the Fritz Haber Institute of the Max Planck Society. In 2020, he became a professor in Hunan University. His research interests are studying two-dimensional materials using tip-enhanced Raman spectroscopy with a resolution of 1 nm or higher based on a scanning tunneling microscope.

## 2. Methods

### Grooved tip design

Prior to tip fabrication, we conducted numerical simulations to examine the geometric parameters of the groove and pyramid shape of the tip shaft, aiming to maximize near-field enhancement at the tip apex under groove illumination. For simplicity, we use a free-standing tip without an Ag substrate in these parametric optimization studies. Fig. 2(a–c) illustrate the tip geometry, indicating five adjustable parameters: the distance between the groove edge and the tip apex ( $L$ ), the width ( $W$ ) and depth ( $D$ ) of the groove, and the apex angles ( $\theta_1$  and  $\theta_2$ ). The value  $L$  of 10  $\mu\text{m}$  ensures sufficient separation between the apex and the

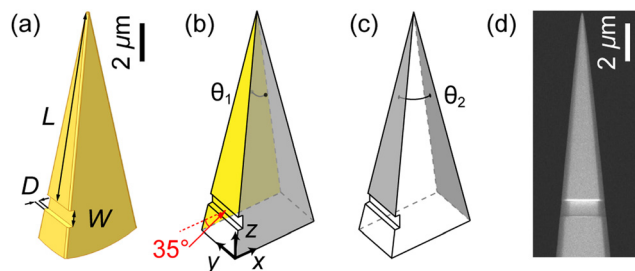


**Fig. 2** Design and fabrication of the grooved pyramid tip. (a–c) Structural parameters of the grooved pyramid tip; the red arrow indicates the central axis of the incident Gaussian beam. (d) SEM image of the fabricated tip.

groove compared to the focal spot size of approximately  $4\ \mu\text{m}$  while minimizing damping of the SPP during propagation from the groove to the apex.<sup>14,49</sup> By evaluating the field enhancement across different parameters, we obtain  $W = 900\ \text{nm}$ ,  $D = 300\ \text{nm}$ ,  $\theta_1 = 10^\circ$  and  $\theta_2 = 20^\circ$  as a nearly optimal combination. We chose the near optimal because we traded some field enhancement for easier fabrication. Fig. 2d shows an SEM of the tip fabricated by focused ion beam milling. The designed tip shape is well reproduced. More details about the tip design, simulation, and fabrication are described in the ESI section 1.†

### Experimental

The experiments were performed in a UHV chamber (base pressure  $<5 \times 10^{-10}$  mbar) equipped with a low-temperature STM (modified UNISOKU USM-1400). The STM bias voltage ( $V$ ) is applied to the Ag(111) sample and the tip is grounded. The Ag(111) surface was cleaned by repeated cycles of  $\text{Ar}^+$  sputtering and annealing up to 670 K, yielding an atomically flat surface. The UHV chamber has fused silica windows for optical access. A CW laser (633 nm or 780 nm) is focused on the STM junction at an angle of  $55^\circ$  with respect to the tip central axis using an *in situ* Ag-coated parabolic mirror mounted on the cryogenic STM stage. The diameter of the incident beam is around 5 mm, and the effective focal length of the parabolic mirror is 8.85 mm. Accurate beam alignment and focusing is achieved by piezo motors (Attocube GmbH) to position the parabolic mirror and to align three translational and two rotational axes. The laser is polarized along the plane spanned by the tip axis and the axis of the laser beam, and the diameter of the focal spot is estimated to be  $6\lambda$  (where  $\lambda$  is the laser wavelength), which is estimated by scanning the focal spot across the tip apex and recording the distance over which the tip apex lights up. The movement of the parabolic mirror (and hence the laser spot) is calibrated from the known distance between the apex and the groove and the scattered light we observe from the junction (inset in Fig. 1).

Turning the laser on or off causes thermal expansion of the tip, disturbing the measurements. To eliminate its impact, all measurements started several minutes after starting or stopping laser illumination, when thermal expansion is no longer detectable. The thermal expansion is monitored by measuring the tip height, *i.e.*, change in the piezoelectric tube length,

while maintaining a constant gap distance through the feedback loop. The differential conductance ( $\partial j/\partial V$ , with  $j$  the tunneling current) spectra are recorded using a lock-in amplifier with 20 mV modulation at a frequency of 983 Hz. All measurements are conducted at 15 K.

## 3. Results and discussion

The insets in Fig. 1 display optical images of light scattered from the groove and the tip-apex. As the laser focal spot is scanned along the tip axis, we observe two intensity maxima in the back-scattered light when the laser spot is at the apex and the groove, respectively. These maxima serve as indicators for precise positioning of the laser spot on the groove or the apex. In Fig. 1b, light scattering is observed from the groove when the tip apex is directly illuminated, indicating that SPPs propagate along the tip shaft and couple to the far-field at the groove. Conversely, the opposite behavior is expected when focusing the laser on the groove. However, strong back-reflection from the groove makes it challenging to observe the scattered light from the apex due to the limited dynamic range of the camera.

Fig. 3a shows  $\partial j/\partial V$  spectra measured under dark conditions (gray) and during 780 nm laser illumination, for the laser being focused on the tip apex (blue curve) and the groove (red curve). In the constant-current mode (CCM) without illumination, we observed the first FER peak at 4.1 V, which corresponds to the image potential state on the Ag(111) surface.<sup>50</sup> Off-site excitation with a 780 nm laser induces a shift in the first FER peak from its original position at  $V_1 = 4.1\ \text{V}$  to  $V'_1 = 2.6\ \text{V}$ , resulting in a difference of  $|\Delta V_1| = 1.5\ \text{V}$ , where  $\Delta V_1 = V'_1 - V_1$  and  $V_1$  and  $V'_1$  represent the position of the first FER peak before and during laser illumination, respectively. The peak shift  $|\Delta V_1| = 1.5\ \text{V}$  under off-site excitation is approximately equals to the incident photon energy of 1.59 eV. When the tip apex is illuminated directly, the first plasmon-assisted FER peak appears at  $V'_1 = 2.9\ \text{V}$ , corresponding to a difference of  $|\Delta V_1| = 1.2\ \text{V}$  relative to the original peak at  $V_1 = 4.1\ \text{V}$ , such that the  $|\Delta V_1|$  is smaller than the incident photon energy. The plasmon-assisted first FER peak arises from a resonant electron tunneling process in which an electron tunneling from the tip gains energy by absorption of a photon, such that it can tunnel into the image potential state at lower bias voltage.<sup>47</sup> The different  $|\Delta V_1|$  between off-site and tip-apex illumination is attributed to an energetic shift of the image potential state due to different gap distances as explained in the ESI Fig. S3a.† Most importantly, we find that the plasmon-assisted first FER peak is stronger under off-site excitation than that under apex illumination, indicating that the near-field intensity is higher than that achieved with direct tip-apex illumination.

In CCM, the gap distance varies with bias voltage as well as different near-field intensity caused by off-site and tip-apex excitation (ESI Fig. S3†), as different bias voltage or near-field intensity result in different photocurrent assuming that the gap distance is constant. To ensure a fair comparison of the

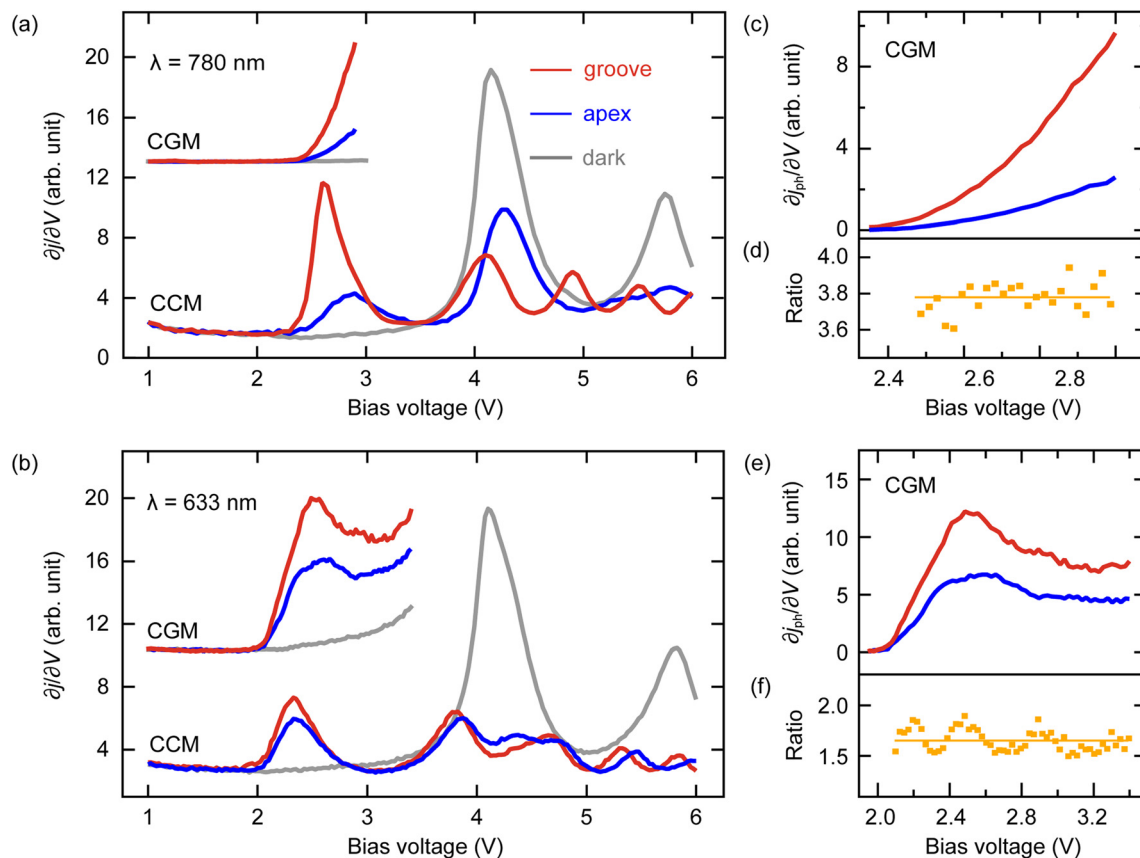


**Fig. 3** (a and b)  $\partial j/\partial V$  spectra acquired on Ag (111) surface under apex (blue) or groove (red) illumination showing FER peaks. The excitation wavelengths are 780 nm ( $h\nu = 1.59$  eV) and 633 nm ( $h\nu = 1.96$  eV), with the laser intensities at the focus are  $9.6 \text{ kW cm}^{-2}$  and  $8.8 \text{ kW cm}^{-2}$ , respectively. The grey curves represent the spectra without illumination. The spectra in constant-current mode (CCM) were acquired with a current setpoint of 0.1 nA. The spectra in constant-gap-distance mode (CGM) were acquired with the gap distance set by a tunneling current of 0.1 nA at 1 V. The CGM spectra are shifted vertically for clarity. (c and e)  $\partial j_{\text{ph}}/\partial V$  spectra acquired at constant gap distance set by a tunneling current of 0.1 nA at 1 V. (d and f) The ratios (orange dots) of  $\partial j_{\text{ph}}/\partial V$  under groove to those under apex illumination. The solid lines indicate the average value.

near-field intensities between the two excitation schemes, it is essential to measure and compare the FER spectra in constant gap-distance mode (CGM) and to maintain the same gap distance across different excitation configurations or across varying illuminating power. We employ the same STM setpoint for all FER measurements (e.g.,  $V = 1$  V and  $j = 0.1$  nA) and verify that photocurrents are negligible at this setpoint, ensuring that the gap distance is determined by the static current after thermal equilibration of the electrons in metals (see ESI Fig. S4† for details). The  $\partial j/\partial V$  spectra in Fig. 3a recorded in CGM show a slope with an onset at  $V \sim 2.4$  V during off-site and tip-apex excitation. The signal is again significantly higher under off-site excitation.

The data in Fig. 3b is measured at an excitation wavelength of 633 nm. In the CCM spectra, illumination causes a shift of the first FER peak by  $|\Delta V_1| = 1.8$  V to  $V_1 = 2.3$  V, with  $|\Delta V_1|$  closely matching the photon energy of 1.96 eV. In the CGM spectra, the plasmon-assisted FER peaks appear at a slightly higher voltage of  $V_1 = 2.5$  V, which we attribute to the energy shift of the image potential state caused by differences in gap distances between the CCM and CGM (ESI Fig. S3b† for details).

To quantitatively compare the near-field intensities of the LSPs excited by tip-apex and off-site excitation, the current in CGM can be expressed as

$$j(V, |E_A|) = j_d(V) + j_{\text{ph}}(V, |E_A|) = j_d(V) + c_1 f_1(V) |E_A|^2, \quad (1)$$

where  $j$  is the total current under illumination,  $j_d$  is dark current,  $E_A$  is the electric field of the LSP at the apex and  $j_{\text{ph}}$  is photocurrent. Assuming that  $V$  and the local field  $E_A$  affect the  $j_{\text{ph}}$  independently, the one-photon photocurrent can be written as a product of a bias-dependent function  $f_1(V)$  and the square amplitude of the local electric field ( $|E_A|^2$ ). The laser intensity dependence of the photocurrent in the ESI Fig. S5† verifies that the first plasmon-assisted FER peak originates from a one-photon process. By taking the derivative of eqn (1), we obtain

$$\frac{\partial j_{\text{ph}}(V, |E_A|)}{\partial V} = \frac{\partial j(V, |E_A|)}{\partial V} - \frac{dj_d(V)}{dV} = c_1 f_1'(V) |E_A|^2. \quad (2)$$

Therefore,  $\frac{\partial j_{\text{ph}}(V, |E_A|)}{\partial V}$  can be determined from the spectra in Fig. 3(a and b) recorded in CGM, which give  $\frac{\partial j}{\partial V}$  and  $\frac{dj_d}{dV}$  for

the illuminated and dark case, respectively.  $\frac{\partial j_{\text{ph}}}{\partial V}$  is plotted in Fig. 3(c and e). Denoting  $|E_{\text{A}}|$  under groove and apex illumination as  $|E_{\text{A}}^{\text{IG}}|$  and  $|E_{\text{A}}^{\text{IA}}|$ , respectively, we derive the following relationship:

$$\frac{\partial j_{\text{ph}}(V, |E_{\text{A}}^{\text{IG}}|)}{\partial V} / \frac{\partial j_{\text{ph}}(V, |E_{\text{A}}^{\text{IA}}|)}{\partial V} = \frac{|E_{\text{A}}^{\text{IG}}|^2}{|E_{\text{A}}^{\text{IA}}|^2}. \quad (3)$$

This shows that the ratio of  $\frac{\partial j_{\text{ph}}}{\partial V}$  measured under groove and tip-apex excitation equals the ratio of the local intensities,  $\frac{|E_{\text{A}}^{\text{IG}}|^2}{|E_{\text{A}}^{\text{IA}}|^2}$ , and is independent of the bias voltage. Fig. 3(d and f) display the ratios plotted *versus* the bias voltage. The average ratios are indicated by the horizontal line. The data points are distributed randomly on both sides of the line, indicating that the ratio is indeed independent on the bias voltage, validating the relationship in eqn (3). We find that the average near-field intensity ratio is  $\frac{|E_{\text{A}}^{\text{IG}}|^2}{|E_{\text{A}}^{\text{IA}}|^2} \approx 3.8$  for the excitation wavelength of 780 nm and 1.7 for 633 nm. We also note that the oscillatory behavior of the ratio in Fig. 3f is due to noise from the lock-in amplifier (ESI Fig. S6†) and does not have any physical meaning.

The fact that the measured intensity ratio is greater than unity indicates that the energy flux directed into the LSP through off-site excitation surpasses that achieved by direct tip-apex excitation. The energy flux (SI unit:  $\text{J s}^{-1}$ ) refers to the rate of energy transfer through a surface (not per unit area). In the groove-coupled off-site excitation, a fraction of far-field energy flux is initially converted into propagating SPPs. During the nanofocusing process, the SPPs are damped by ohmic loss and radiating into the far-field, and some remaining energy is converted into LSPs creating a localized field inside the STM junction. The far- to near-field conversion efficiency is defined as the fraction of total incident energy flux that is directed into the near-field region inside the STM junction. Since the size of the near-field is the same under both excitation scheme, the ratio of conversion efficiency for off-site *versus* tip-apex excitation equals the ratio of the near-field intensity.<sup>16</sup> The larger conversion efficiency observed for off-site excitation can be attributed to the larger geometric cross-section of the groove, fitting the size of laser focal spot better, and compensates for the additional SPP loss. Last, it worths mentioning that the intensity ratio of 3.8 at the excitation wavelength of 780 nm in this study is only slightly lower than the reported intensity ratio of 4.4 achieved for gratings at 785 nm wavelength.<sup>16,‡</sup>

To further demonstrate the sensitivity of the intensity of the FER peak to the change of the near-field intensity, we examine the variation of plasmon-induced  $\partial j_{\text{ph}}/\partial V$  signal as the

laser focal spot is scanned along the tip axis (Fig. 4a). Fig. 4b displays the  $\partial j/\partial V$  spectra in CGM obtained at various focal positions along the tip. The first plasmon-assisted FER peak at  $V = 2.5$  V appears when the laser is focused on either the groove or the apex. Fig. 4c shows the resulting photocurrent and  $\partial j_{\text{ph}}/\partial V (= \partial j/\partial V - dj_{\text{d}}/dV)$  at 2.5 V as a function of the focal position. The  $\partial j_{\text{ph}}/\partial V$  spectra exhibit features of plasmon-assisted FER when the laser is focused on either the groove or the apex, but these features are absent when the focal spot is positioned between them. The plasmon-induced  $\partial j_{\text{ph}}/\partial V$ , which directly reflects the near-field intensity in the junction, is sensitive to a change of the laser focal position of approximately 1  $\mu\text{m}$ . This sensitivity suggests that the plasmon-assisted FER peak serves as a reliable indicator for precise optimization of the beam position on the tip.

To obtain further insights into the differences between the groove and apex illumination, we simulated the distributions of electric-field enhancement for both configurations. Fig. 5 presents the results for an excitation wavelength of 780 nm. The electric-field enhancement factor under groove (apex) illumination is defined as  $|E_{\text{A}}^{\text{IG(A)}}|/|E_{\text{laser}}|$ , where  $|E_{\text{laser}}|$  denote the electric-field amplitude of the incident laser at the center of the focal spot. Since  $|E_{\text{laser}}|$  is identical for both groove and apex illumination, the ratio of field enhancement factors is equivalent to the ratio of the electric-field amplitudes  $|E_{\text{A}}^{\text{IG}}|/|E_{\text{A}}^{\text{IA}}|$ . Fig. 5(a and b) compare the spatial distribution of the field enhancement along the surface of the pyramid tip. In the case of off-site excitation, a small fraction of the nanofocused SPPs reflects back from the apex and interferes with the counter-propagating SPPs along the shaft, forming weak interference fringes. In contrast, only weak SPP intensity and interference effects are observed for direct illumination of the tip apex, because the SPPs diverge, and their intensity decreases during propagating towards the groove. Fig. 5(c and d) show that the maximum field enhancement occurs at the atomic-scale protrusion under both groove and apex illumination. Notably, the field enhancement at the atomic-scale protrusion is significantly higher under groove illumination compared to apex illumination, further supporting the superior efficiency of groove-coupled off-site excitation in concentrating the field enhancement at the junction.

Table 1 lists the field enhancement factors on the vacuum side of the tip apex under both off-site and tip-apex excitation. These values quantify the amplification of the electric field at the apex with the respective excitation schemes. The field enhancement factors reach several hundred within the gap formed between the tip and the Ag surface and are further amplified by approximately five-fold with the addition of an atomic-scale protrusion (picocavity) with both excitation schemes. At an excitation wavelength of 780 nm, the ratio of the near-field intensity under off-site excitation to that under tip-apex excitation is approximately 6.6, irrespective of the presence/absence of the atomic-scale protrusion. This confirms that the efficiency of groove-coupled off-site excitation of the LSP significantly surpasses that of direct tip-apex illumination. At the excitation wavelength of 633 nm, the simulated

‡ The TERS intensity is proportional to the fourth power of the electric-field amplitude, so we determined the near-field intensity ratio between grating and apex illumination to be approximately 4.4 after taking the square root of the ratio of TERS intensities, which is approximately 20 in the reference.

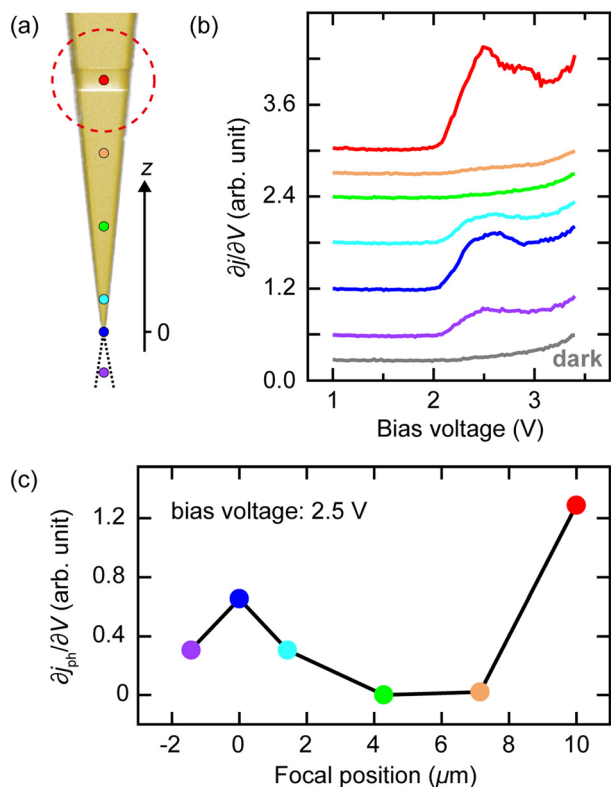


**Fig. 4** (a) Laser-spot positions for spectra acquisition along the tip axis. A SEM image of the tip is used for illustration purpose. The dashed circle illustrates the size of the focused beam. The purple dot means the laser spot at the mirror image of the tip (dashed outline). (b)  $dI/dV$  spectra obtained at the focal positions marked in (a) with a 633 nm excitation wavelength. The spectra were recorded in the constant gap-distance mode at a gap distance set by  $V = 1$  V and  $j = 0.1$  nA. (c)  $dI_{ph}/dV$  at  $V = 2.5$  V as a function of focal position.

ratio of the near-field intensity for off-site *versus* tip-apex excitation decreases to approximately 4.6. The smaller value than that obtained for 780 nm is attributed to higher damping and ohmic loss for SPPs at higher frequencies.<sup>49</sup> The experimental ratios in the last column of the table are lower than the simulated predictions, corresponding to approximately 39% and 57% of the simulated values at excitation wavelengths of 633 nm and 780 nm, respectively. This discrepancy arises from additional SPP scattering losses caused by surface roughness during nanofocusing in experiments, whereas the simulations assume an idealized, perfectly smooth pyramid surface with minimal scattering.

The exceptional performance of the grooved tip relies on careful optimization of its geometric parameters through simulations. Below, we outline this optimization process, focusing on the relationship between field enhancement at the tip apex and the grooved tip's geometry. Fig. 6(a–d) shows two-dimensional plots of the electric-field enhancement  $|E_A|/|E_{laser}|$ , where  $|E_A|$  is taken from the vacuum side of the tip apex. Fig. 6(a and b) explore various combinations of groove widths ( $W$ ) ranging from 100 nm to 1000 nm and depths ( $D$ )

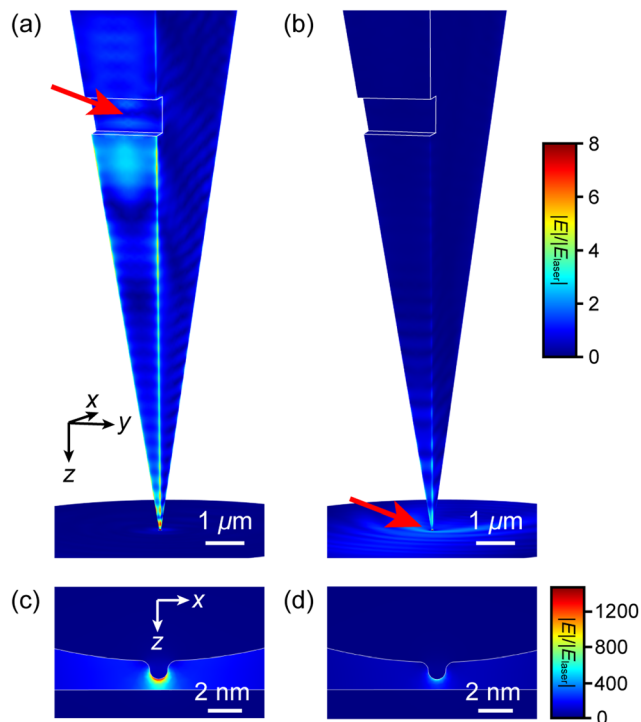


**Fig. 5** Distributions of the enhancement factor under groove (a and c) and apex (b and d) illumination at an excitation wavelength of 780 nm. The incident wave vector (red arrow) is in the  $x$ – $z$  plane and forms an angle of  $35^\circ$  with respect to the horizontal plane.

**Table 1** Field enhancement factors at the tip apex under groove and apex illumination, along with the ratios of near-field intensities

$\lambda$ (nm)	$ E_A^G / E_{laser} $ Simulation	$ E_A^{iA} / E_{laser} $ Simulation	$ E_A^G ^2/ E_A^{iA} ^2$ Simulation	$ E_A^G ^2/ E_A^{iA} ^2$ Experiment
633	1218 (239)	568 (108)	4.6 (4.9)	1.7
780	1426 (383)	556 (148)	6.6 (6.7)	3.8

The simulated enhancement factors without parentheses are taken from the vacuum side of the protrusions for tip apices with atomic-scale protrusions, while the values in parentheses are from the vacuum side of the tip apices without protrusions.

ranging from 100 nm to 500 nm at the excitation wavelengths of 780 nm and 633 nm, respectively. The groove distance ( $L = 10 \mu\text{m}$ ) and apex angles ( $\theta_1 = 10^\circ$  and  $\theta_2 = 20^\circ$ ) are kept constant. The simulation results are in general agreement with a previous theoretical study on SPP excitation with a single groove,<sup>51</sup> validating the approach and underlying principles of our analysis. At the excitation wavelength of 780 nm, the highest enhancement factors of 19.3 and 19.0 are obtained at  $W = 800$  nm,  $D = 300$  nm and  $W = 900$  nm,  $D = 300$  nm, respectively. At the excitation wavelength of 633 nm, the best enhancement factors of 8.1, 8.0, and 7.8 occur at  $W = 1000$  nm,  $D = 200$  nm,  $W = 1000$  nm,  $D = 300$  nm and  $W = 900$  nm,  $D = 300$  nm, respectively. Therefore, the combination of  $W = 900$  nm and  $D = 300$  nm is selected as it gives one of the best enhancements at both wavelengths.

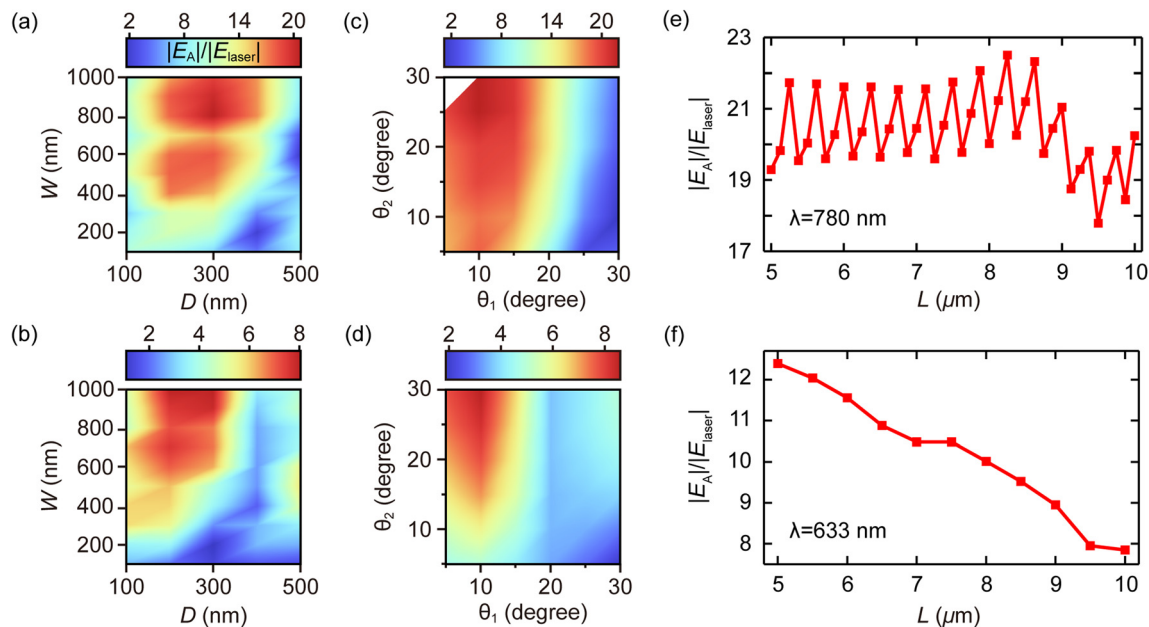


**Fig. 6** Enhancement factor of electric field at the tip apex as a function of (a and b) groove width  $W$  and depth  $D$ , (c and d) apex angles  $\theta_1$  and  $\theta_2$ , and (e and f) groove-to-apex distance  $L$ . Fixed parameters: (a and b)  $\theta_1 = 10^\circ$ ,  $\theta_2 = 20^\circ$ , and  $L = 10 \mu\text{m}$ . (c and d)  $W = 900 \text{ nm}$ ,  $D = 300 \text{ nm}$ , and  $L = 10 \mu\text{m}$ . (e and f)  $\theta_1 = 10^\circ$ ,  $\theta_2 = 20^\circ$ ,  $W = 900 \text{ nm}$ , and  $D = 300 \text{ nm}$ . The excitation wavelength is  $780 \text{ nm}$  in (a, c and e) and  $633 \text{ nm}$  in (b, d and f).

Next, the apex angles are optimized with fixed values of  $W = 900 \text{ nm}$  and  $D = 300 \text{ nm}$ . In general, the angle  $\theta_1$  has a greater influence on the enhancement factor than  $\theta_2$ , as shown in Fig. 6(c and d). Decreasing  $\theta_1$  enhances the nanofocusing effect,<sup>52</sup> however, it also reduces groove's  $y$ -direction length ( $L_y$ ), which in turn reduces the laser radiation received by the groove. At  $\theta_1 = 25^\circ$ , the  $L_y$  becomes comparable to the diameter of the focused beam. Initially, as  $\theta_1$  decreases, the enhancement factor increases because the enhanced adiabatic nanofocusing dominates. However, when  $\theta_1$  drops below  $10^\circ$ , the reduction in the laser radiation received by the groove becomes dominant, leading to a decrease in the enhancement factor. The maximum enhancement factors are achieved at  $\theta_1 = 10^\circ$ ,  $\theta_2 = 25^\circ$  and  $\theta_1 = 10^\circ$ ,  $\theta_2 = 30^\circ$  for the excitation wavelengths of  $780 \text{ nm}$  and  $633 \text{ nm}$ , respectively. We select  $\theta_1 = 10^\circ$  and  $\theta_2 = 20^\circ$  because this combination is easier to fabricate due to a smaller difference between  $\theta_1$  and  $\theta_2$ . The enhancement factor at  $\theta_1 = 10^\circ$  and  $\theta_2 = 20^\circ$  corresponds to approximately 90% of the maximum enhancement factor at both excitation wavelengths. In conclusion, we obtain  $W = 900 \text{ nm}$ ,  $D = 300 \text{ nm}$ ,  $\theta_1 = 10^\circ$  and  $\theta_2 = 20^\circ$  as a near-optimal combination.

As discussed above, the groove–apex distance ( $L$ ) is fixed at  $10 \mu\text{m}$ . Subsequently, we investigate the influence of  $L$  on the field enhancement at the tip apex, as shown in Fig. 6(e and f). At the excitation wavelength of  $780 \text{ nm}$ , the field enhancement oscillates with a periodicity of approximately  $\lambda/2$  as  $L$  varies from  $5 \mu\text{m}$  to  $10 \mu\text{m}$ . This is attributed to the interference within the Fabry–Pérot cavity formed between the groove and the tip apex. Notably, the peak values of the oscillations remain nearly constant as  $L$  varies from  $5 \mu\text{m}$  to  $9 \mu\text{m}$ . In contrast, at the excitation wavelength of  $633 \text{ nm}$ , the field

enhancement decays significantly as  $L$  varies from  $5 \mu\text{m}$  to  $10 \mu\text{m}$ . The observed difference between the two wavelengths arises from the different SPP decay lengths ( $L_{\text{SPP}}$ ). At  $780 \text{ nm}$ , the  $L_{\text{SPP}}$  is substantially longer than  $L$ .<sup>53</sup> As  $L$  increases,  $L_y$  increases, allowing the groove to capture more radiation to compensate for SPP losses. Conversely, at  $633 \text{ nm}$ ,  $L_{\text{SPP}}$  is comparable to  $L$ ,<sup>53</sup> causing SPP loss dominating as  $L$  increases. Therefore, the performance of the grooved tip can be further improved by reducing  $L$ .

## 4. Conclusions

In summary, we developed a novel method for comparing near-field intensity under different excitation schemes in an STM junction using plasmon-assisted FERs. We applied this approach to evaluate the field enhancement of a plasmonic picocavity in a low-temperature STM, resulting from an off-site excitation *via* plasmonic nanofocusing. We fabricated a grooved pyramid tip with nearly optimized geometric parameters that are  $W = 900 \text{ nm}$ ,  $D = 300 \text{ nm}$ ,  $\theta_1 = 10^\circ$  and  $\theta_2 = 20^\circ$  and quantified ratio of near-field intensity at the tip apex under off-site excitation relative to that under direct tip-apex excitation. At an excitation wavelength of  $780 \text{ nm}$ , the ratio of the near-field intensities under groove and apex illumination is close to 3.8, reaching 57% of the theoretical value. At the excitation wavelength of  $633 \text{ nm}$ , the ratio is 1.7, which corresponds to 38% of the theoretical value but is still greater than unity. These suggest that the grooved pyramidal tip is suitable for multi-wavelength excitations. Prospectively, the grooved pyramidal tip offers a relatively simple structure for tip-

enhanced optical spectroscopy by effectively suppressing the significant far-field contributions, paving the way for more precise and background-free near-field spectroscopic studies.

## Author contributions

Chenfang Lin: investigation; methodology (equal); formal analysis (equal); supervision (equal); writing – review & editing (equal). Jie Li: formal analysis (equal); writing – original draft (equal). Guoao Li: methodology (equal). Wenjie Luo: writing – original draft (equal). Shuyi Liu: resources (equal). Adnan Hammud: resources (equal). Yang Xia: resources (equal). Anlian Pan: resources (equal). Martin Wolf: resources (equal). Melanie Müller: writing – review & editing (auxiliary); supervision (equal). Takashi Kumagai: conceptualization; funding acquisition; supervision (equal); writing – review & editing (equal).

## Data availability

Data for this article are available at Zenodo at <https://doi.org/10.5281/zenodo.14600345>.

## Conflicts of interest

There are no conflicts to declare.

## Acknowledgements

The authors thank Hiroko Yoshino for supporting the experiments. T. K. acknowledges a support by JST FOREST Program (Grant Number JPMJFR201J, Japan). C. L. acknowledges the support by the National Key Research and Development Program of China (No. 2022YFA1204700), the National Natural Science Foundation of China (No. 12104146), the Natural Science Foundation of Hunan Province (No. 2022JJ20002), and the Fundamental Research Funds for the Central Universities (No. 227202101005, 227202201293).

## References

- 1 R. Gutzler, M. Garg, C. R. Ast, K. Kuhnke and K. Kern, *Nat. Rev. Phys.*, 2021, **3**, 441–453.
- 2 R. Zhang, Y. Zhang, Z. C. Dong, S. Jiang, C. Zhang, L. G. Chen, L. Zhang, Y. Liao, J. Aizpurua, Y. Luo, J. L. Yang and J. G. Hou, *Nature*, 2013, **498**, 82–86.
- 3 J. Lee, K. T. Crampton, N. Tallarida and V. A. Apkarian, *Nature*, 2019, **568**, 78–82.
- 4 B. Yang, G. Chen, A. Ghafoor, Y. Zhang, Y. Zhang, Y. Zhang, Y. Luo, J. Yang, V. Sandoghdar, J. Aizpurua, Z. Dong and J. G. Hou, *Nat. Photonics*, 2020, **14**, 693–699.
- 5 M. Imai-Imada, H. Imada, K. Miwa, Y. Tanaka, K. Kimura, I. Zoh, R. B. Jaculbia, H. Yoshino, A. Muranaka, M. Uchiyama and Y. Kim, *Nature*, 2022, **603**, 829–834.
- 6 J. Y. Xu, X. Zhu, S. J. Tan, Y. Zhang, B. Li, Y. Z. Tian, H. Shan, X. F. Cui, A. D. Zhao, Z. C. Dong, J. L. Yang, Y. Luo, B. Wang and J. G. Hou, *Science*, 2021, **371**, 818–822.
- 7 Y. Park, I. Hamada, A. Hammud, T. Kumagai, M. Wolf and A. Shiotari, *Nat. Commun.*, 2024, **15**, 6709.
- 8 Q. Meng, J. Zhang, Y. Zhang, W. Chu, W. Mao, Y. Zhang, J. Yang, Y. Luo, Z. Dong and J. G. Hou, *Sci. Adv.*, 2024, **10**, ead11015.
- 9 B. Cirera, M. Wolf and T. Kumagai, *ACS Nano*, 2022, **16**, 16443–16451.
- 10 F. Benz, M. K. Schmidt, A. Dreismann, R. Chikkaraddy, Y. Zhang, A. Demetriadou, C. Carnegie, H. Ohadi, B. de Nijs, R. Esteban, J. Aizpurua and J. J. Baumberg, *Science*, 2016, **354**, 726–729.
- 11 J. J. Baumberg, *Nano Lett.*, 2022, **22**, 5859–5865.
- 12 M. Urbietta, M. Barbry, Y. Zhang, P. Koval, D. Sanchez-Portal, N. Zabala and J. Aizpurua, *ACS Nano*, 2018, **12**, 585–595.
- 13 T. L. Vasconcelos, B. S. Archanjo, B. Fragneaud, B. S. Oliveira, J. Riikonen, C. Li, D. S. Ribeiro, C. Rabelo, W. N. Rodrigues, A. Jorio, C. A. Achete and L. G. Cancado, *ACS Nano*, 2015, **9**, 6297–6304.
- 14 H. Bockmann, M. Muller, A. Hammud, M. G. Willinger, M. Pszona, J. Waluk, M. Wolf and T. Kumagai, *J. Phys. Chem. Lett.*, 2019, **10**, 2068–2074.
- 15 F. Lu, W. Zhang, M. Liu, L. Zhang and T. Mei, *IEEE J. Sel. Top. Quantum Electron.*, 2021, **27**, 1–12.
- 16 S. Berweger, J. M. Atkin, R. L. Olmon and M. B. Raschke, *J. Phys. Chem. Lett.*, 2010, **1**, 3427–3432.
- 17 A. J. Babadjanyan, N. L. Margaryan and K. V. Nerkararyan, *J. Appl. Phys.*, 2000, **87**, 3785–3788.
- 18 M. I. Stockman, *Phys. Rev. Lett.*, 2004, **93**, 137404.
- 19 C. Ropers, C. C. Neacsu, T. Elsaesser, M. Albrecht, M. B. Raschke and C. Lienau, *Nano Lett.*, 2007, **7**, 2784–2788.
- 20 S. Berweger, J. M. Atkin, R. L. Olmon and M. B. Raschke, *J. Phys. Chem. Lett.*, 2012, **3**, 945–952.
- 21 T. Umakoshi, M. Tanaka, Y. Saito and P. Verma, *Sci. Adv.*, 2020, **6**, eaba4179.
- 22 C. C. Neacsu, S. Berweger, R. L. Olmon, L. V. Saraf, C. Ropers and M. B. Raschke, *Nano Lett.*, 2010, **10**, 592–596.
- 23 K. Zhang, S. I. Taniguchi and T. Tachizaki, *Opt. Lett.*, 2018, **43**, 5937–5940.
- 24 K. V. Nerkararyan, *Phys. Lett. A*, 1997, **237**, 103–105.
- 25 D. K. Gramotnev and S. I. Bozhevolnyi, *Nat. Photonics*, 2013, **8**, 13–22.
- 26 M. Esmann and C. Lienau, *Microsc. Anal.*, 2020, **47**, 22–23.
- 27 D. Xu, B. Liang, Y. Xu and M. Liu, *Nano Res.*, 2022, **16**, 5555–5571.
- 28 A. Wöste, G. Hergert, T. Quenzel, M. Silies, D. Wang, P. Groß and C. Lienau, *Nano Lett.*, 2023, **23**, 5528–5534.

- 29 W. Luo, R. Song, B. G. Whetten, D. Huang, X. Cheng, A. Belyanin, T. Jiang and M. B. Raschke, *Small*, 2024, **20**, 2307345.
- 30 W. Luo, B. G. Whetten, V. Kravtsov, A. Singh, Y. Yang, D. Huang, X. Cheng, T. Jiang, A. Belyanin and M. B. Raschke, *Nano Lett.*, 2023, **23**, 1767–1773.
- 31 T. Jiang, V. Kravtsov, M. Tokman, A. Belyanin and M. B. Raschke, *Nat. Nanotechnol.*, 2019, **14**, 838–843.
- 32 T. Umakoshi, Y. Saito and P. Verma, *Nanoscale*, 2016, **8**, 5634–5640.
- 33 K. Tomita, Y. Kojima and F. Kannari, *Nano Lett.*, 2018, **18**, 1366–1372.
- 34 X. Ma, Y. Zhu, N. Yu, S. Kim, Q. Liu, L. Apontti, D. Xu, R. Yan and M. Liu, *Nano Lett.*, 2019, **19**, 100–107.
- 35 K. Zhang, Y. Bao, M. Cao, S.-I. Taniguchi, M. Watanabe, T. Kambayashi, T. Okamoto, M. Haraguchi, X. Wang, K. Kobayashi, H. Yamada, B. Ren and T. Tachizaki, *Anal. Chem.*, 2021, **93**, 7699–7706.
- 36 V. Kravtsov, R. Ulbricht, J. M. Atkin and M. B. Raschke, *Nat. Nanotechnol.*, 2016, **11**, 459–464.
- 37 G. A. Traeger, M. H. Teichmann, B. Schröder and M. Wenderoth, *Rev. Sci. Instrum.*, 2023, **94**, 023702.
- 38 B. Pettinger, P. Schambach, C. J. Villagomez and N. Scott, *Annu. Rev. Phys. Chem.*, 2012, **63**, 379–399.
- 39 A. Shiotari, T. Kumagai and M. Wolf, *J. Phys. Chem. C*, 2014, **118**, 11806–11812.
- 40 H. An, J. Li, Y. Liu, P. Xu, S. Han, Y. Liu, S. Chen, S.-Y. Li, C. Lin and A. Pan, *J. Phys. Chem. C*, 2024, **128**, 7583–7590.
- 41 K.-D. Park, O. Khatib, V. Kravtsov, G. Clark, X. Xu and M. B. Raschke, *Nano Lett.*, 2016, **16**, 2621–2627.
- 42 A. Shiotari, J. Nishida, A. Hammud, F. Schulz, M. Wolf, T. Kumagai and M. Müller, *arXiv*, 2024, preprint, arXiv:2410, p. 18455, DOI: [10.48550/arXiv.2410.18455](https://doi.org/10.48550/arXiv.2410.18455).
- 43 S. Liu, F. P. Bonafe, H. Appel, A. Rubio, M. Wolf and T. Kumagai, *ACS Nano*, 2023, **17**, 10172–10180.
- 44 M. Müller, V. Kravtsov, A. Paarmann, M. B. Raschke and R. Ernstorfer, *ACS Photonics*, 2016, **3**, 611–619.
- 45 J. Vogelsang, J. Robin, B. J. Nagy, P. Dombi, D. Rosenkranz, M. Schiek, P. Gross and C. Lienau, *Nano Lett.*, 2015, **15**, 4685–4691.
- 46 B. Schröder, O. Bunjes, L. Wimmer, K. Kaiser, G. A. Traeger, T. Kotzot, C. Ropers and M. Wenderoth, *New J. Phys.*, 2020, **22**, 033047.
- 47 S. Liu, M. Wolf and T. Kumagai, *Phys. Rev. Lett.*, 2018, **121**, 226802.
- 48 X.-B. Zhang, Y.-F. Zhang, H. Li, J. Cui, S. Jiang, B. Yang, Y. Zhang, Y. Zhang and Z.-C. Dong, *Chin. J. Chem. Phys.*, 2022, **35**, 713–719.
- 49 H. Bockmann, S. Liu, M. Muller, A. Hammud, M. Wolf and T. Kumagai, *Nano Lett.*, 2019, **19**, 3597–3602.
- 50 T. Kumagai, S. Liu, A. Shiotari, D. Baugh, S. Shaikhutdinov and M. Wolf, *J. Phys.: Condens. Matter*, 2016, **28**, 494003.
- 51 J. Renger, S. Grafström and L. M. Eng, *Phys. Rev. B: Condens. Matter Mater. Phys.*, 2007, **76**, 045431.
- 52 R. Yadav, T. Umakoshi and P. Verma, *AIP Adv.*, 2022, **12**, 085216.
- 53 M. Kuttge, E. J. R. Vesseur, J. Verhoeven, H. J. Lezec, H. A. Atwater and A. Polman, *Appl. Phys. Lett.*, 2008, **93**, 113110.